

# Magnetic characterization of micropatterned Nd–Fe–B hard magnetic films using scanning Hall probe microscopy

M. Kustov,<sup>1,2,a)</sup> P. Laczkowski,<sup>1</sup> D. Hykel,<sup>1</sup> K. Hasselbach,<sup>1</sup> F. Dumas-Bouchiat,<sup>1</sup> D. O'Brien,<sup>1</sup> P. Kauffmann,<sup>2</sup> R. Grechishkin,<sup>3</sup> D. Givord,<sup>1</sup> G. Reyne,<sup>2</sup> O. Cugat,<sup>2</sup> and N. M. Dempsey<sup>1</sup>

<sup>1</sup>Institut Néel, CNRS-UJF, 25 rue des Martyrs, 38042 Grenoble, France

<sup>2</sup>G2Elab, Electrical Engineering Laboratory, 38402 St Martin d'Hères, France

<sup>3</sup>Laboratory of Magnetoelectronics, Tver State University, 170000 Tver, Russia

(Received 26 May 2010; accepted 5 August 2010; published online 23 September 2010)

Scanning Hall probe microscopy has been used for the quantitative measurement of the  $z$ -component (out-of-plane) of the stray magnetic fields produced by Nd–Fe–B hard magnetic films patterned at the micron scale using both topographic and thermomagnetic methods. Peak-to-peak field values in the range 20–120 mT have been measured at scan heights of 25–30  $\mu\text{m}$  above the samples. Quantitative comparison between calculated and measured field profiles gives nondestructive access to the micromagnets' internal magnetic structure. In the case of topographically patterned films the average value of remanent magnetization is extracted; in the case of thermomagnetically patterned films the depth of magnetization reversal is estimated. The measured field profiles are used to derive the spatial variation in the field and field gradient values at distances in the range 0.1–10  $\mu\text{m}$  above the micromagnet arrays. These length-scales are relevant to the application of the micromagnet arrays for lab-on-chip applications (trapping and confinement of magnetic particles). Very large field and field gradient values as high as 1.1 T and  $4.1 \times 10^6$  T/m, respectively, are estimated. © 2010 American Institute of Physics.

[doi:10.1063/1.3486513]

## I. INTRODUCTION

Integrated micromagnets have many potential applications in various types of magnetic microsystems. They may operate as sensors, actuators, motors, levitation/trapping devices, generators, or switches and have applications in fields as diverse as electronics, telecommunications, automotive and aerospace, astronomy, medicine, biotechnology, and logistics.<sup>1–6</sup> In a first step toward their fabrication, triode sputtering has been shown to be suitable for the preparation of thick films ( $>1 \mu\text{m}$ ) of high performance rare earth-transition metal (RE-TM) materials (Sm–Co, Sm–Co–Cu–Fe–Zr, Nd–Fe–B) over large surface areas.<sup>7–12</sup> To produce the magnetic field distributions and field gradients required in microsystems, the hard magnetic films need to be laterally patterned on the micron-scale. Such patterning of thick RE-TM films has been achieved using microfabrication techniques such as lithography, etching, planarization,<sup>13–16</sup> and more recently using thermomagnetic patterning.<sup>17</sup> Quantitative characterization of the stray fields produced by micropatterned thick hard magnetic films is needed to assess the magnetic quality of the micromagnets as well as to optimize the design of microsystems incorporating these micromagnets. Both magneto-optic imaging using magneto-optic indicator films (MOIFs)<sup>18</sup> and scanning Hall probe microscopy (SHPM) have been developed for the characterization of stray magnetic fields.<sup>19–22</sup> For the specific case of magnetized micropatterned high performance hard magnetic films, magneto-optic imaging using planar MOIF has been

used.<sup>23,24</sup> In this paper we describe the use of a SHPM to measure the stray fields produced by micropatterned hard magnetic Nd–Fe–B films of thickness in the range 4–38  $\mu\text{m}$ , destined for use in magnetic microsystems. The measurements are compared with calculations so as to assess, in a nondestructive manner, the influence of micropatterning on the films' magnetic microstructure (average remanent magnetization,  $\mu$ -magnet volume). Finally, the spatial variation in field and field gradient are compared for two different types of micromagnet arrays.

## II. EXPERIMENTAL DETAILS

### A. Preparation of microstructured hard magnet films

NdFeB films were deposited by high rate triode sputtering onto thermally oxidized Si substrates. The films were deposited at a substrate temperature of 450 °C, and subsequently annealed at 750 °C for 10 min, so as to induce an out-of-plane texture.<sup>11</sup> 100 nm Ta layers were deposited as buffer and capping layers to prevent diffusion into the substrate and oxidation of the hard magnetic layer. The films were patterned at the micron scale using either topographic or thermomagnetic patterning (Fig. 1). The latter technique exploits the fact that when we heat a hard magnetic film we reduce its coercivity. A magnetized film is locally heated by

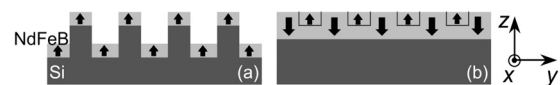


FIG. 1. Schematic side-view representation of (a) topographically and (b) thermomagnetically patterned films.

<sup>a)</sup>Electronic mail: mikhael.kustov@g2elab.grenoble-inp.fr.

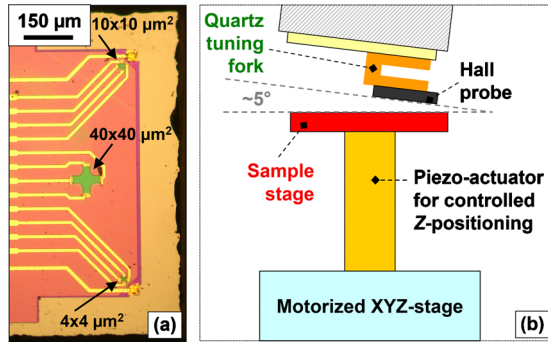


FIG. 2. (Color online) (a) Plan-view image of the Hall probe containing three active areas; (b) schematic diagram of the scanning Hall probe microscope set-up.

laser irradiation through a mask, in the presence of an external magnetic field which is weaker than the film's room temperature value of coercivity. Only those sections of the film which are heated are remagnetized in the direction of the applied field. More details of the technique can be found elsewhere.<sup>17</sup> In the case of topographic patterning, 38  $\mu\text{m}$  thick films were deposited and annealed on Si substrates structured using deep-reactive ion etching (DRIE), and then unidirectionally magnetized out-of-plane.<sup>25</sup> In the case of thermomagnetic patterning, 4  $\mu\text{m}$  thick NdFeB films were patterned in the out-of-plane direction through a mask containing 50  $\mu\text{m}$  wide stripes.<sup>17</sup>

Both the topographically and thermomagnetically patterned films had coercivity values of about 1400 kA/m.

## B. Scanning Hall probe microscope

Second-generation quantum-well Hall sensors based on a two-dimensional (2D) electron gas<sup>26</sup> were used to measure the  $z$ -component of the stray magnetic field patterns above the micropatterned films. The probe used here contains three Hall crosses of active area size  $4 \times 4$ ,  $10 \times 10$ , and  $40 \times 40 \mu\text{m}^2$  [Fig. 2(a)].<sup>27</sup> Figure 2(b) shows a schematic diagram of the scanning Hall probe microscope set-up. The probe is glued onto a commercial quartz tuning fork which serves as a contact sensor in a way similar to that used in the design of a superconducting quantum interference device force microscope.<sup>28</sup> The sample stage is attached to a piezo-actuator, the vertical position of which can be varied in the range of 30  $\mu\text{m}$ . The voltage on the piezoactuator is regulated by a closed-loop proportional-integral-derivative (PID) control where the amplified amplitude of the signal from the tuning fork is supplied to the input of the PID. The piezoactuator and sample stage is fixed on a set of three stepper-motors, allowing the controlled positioning of the sample stage in three directions ( $x, y, z$ ) with a spatial resolution of 0.1  $\mu\text{m}$ .

To prevent damage to the Hall crosses by contact with the sample, the probe is slightly inclined with respect to the sample stage. The inclination angle (typically  $5 \pm 0.5^\circ$ ) was measured optically. Since the inclination angle is relatively small, the measured signal was taken to be the vertical component of the film's stray magnetic field. Knowing the inclination angle and the distance between the edge of the probe

and the center of the Hall cross, the distance between the Hall cross and the surface of the sample being measured was deduced. The magnetic field resolution of the probe was estimated to be better than 10  $\mu\text{T}$  (at the frequency 1000 Hz and the time constant 5 ms) in the measurement range  $< 1 \text{ T}$  but taking into account the system noise during scanning, the magnetic field accuracy was about 100  $\mu\text{T}$ .

## C. Calculation of stray field patterns produced by microstructured magnetic films

The magnetic field patterns generated by microstructured magnetic films have been calculated using the model of equivalent Amperian currents.<sup>29–31</sup> This model, which assumes rigid magnetization patterns, is applicable to the thin film magnets studied here since they are highly coercive and strongly out-of-plane textured (i.e., the film's magnetization may be considered to remain uniform, even in the presence of large demagnetizing fields, although the induction may be nonuniform). This rigidity of magnetization also allows the application of superposition principles for systems composed of many elements.

For the case of an equivalent solenoid in the form of a rectangular prism  $2a \times 2b \times 2h$ , representing a prismatic magnet magnetized along the  $z$ -axis, the magnetic induction for values at any point of observation  $P(x_0, y_0, z_0)$  can be expressed by the following analytical expressions:

$$B_x = -\frac{\mu_0 I}{4\pi 2h} \left\{ \left[ \ln(\beta + \sqrt{\alpha^2 + \beta^2 + \gamma^2}) \right]_{\alpha_1}^{\alpha_2} \beta_2 \gamma_2 \right\},$$

$$B_y = -\frac{\mu_0 I}{4\pi 2h} \left\{ \left[ \ln(\alpha + \sqrt{\alpha^2 + \beta^2 + \gamma^2}) \right]_{\alpha_1}^{\alpha_2} \beta_2 \gamma_2 \right\},$$

$$B_z = -\frac{\mu_0 I}{4\pi 2h} \left[ \left( \arctan \frac{\gamma \sqrt{\alpha^2 + \beta^2 + \gamma^2}}{\alpha \beta} \right)_{\alpha_1}^{\alpha_2} \beta_2 \right]_{\beta_1}^{\gamma_2},$$

$B_x$ ,  $B_y$ , and  $B_z$  are functions,  $f$ , of  $\alpha$ ,  $\beta$ , and  $\gamma$  which obey the following relations:

$$\begin{aligned} \left\{ \left[ f(\alpha, \beta, \gamma) \right]_{\alpha_1}^{\alpha_2} \beta_2 \gamma_2 \right\} &= f(\alpha_2, \beta_2, \gamma_2) - f(\alpha_1, \beta_2, \gamma_2) \\ &\quad - f(\alpha_2, \beta_1, \gamma_2) + f(\alpha_1, \beta_1, \gamma_2) \\ &\quad - f(\alpha_2, \beta_2, \gamma_1) + f(\alpha_1, \beta_2, \gamma_1) \\ &\quad + f(\alpha_2, \beta_1, \gamma_1) - f(\alpha_1, \beta_1, \gamma_1), \end{aligned}$$

and  $\alpha_{1,2} = x_0 \pm a$ ,  $\beta_{1,2} = y_0 \pm b$ ,  $\gamma_{1,2} = z_0 \pm h$  (+ and - signs apply to subscripts 1 and 2, respectively).

The equivalent current  $I$  is to be replaced by  $2hB_r/\mu_0$ , where  $B_r$  is the permanent magnet's remanence.

In the cases where the calculations were compared with SHPM measurements, the sensor's active area is taken into account by assuming that the sensor response is proportional to the average magnetic field in the active area (total magnetic flux divided by the active area).

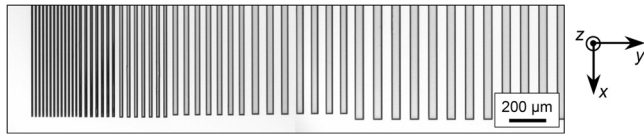


FIG. 3. Optical plan-view image of a part of the topographically patterned substrate.

### III. RESULTS AND DISCUSSION

#### A. Characterization of topographically patterned films

An optical plan-view image of the topographically patterned substrate is shown in Fig. 3. The patterned substrate has etched features of a constant depth  $40\ \mu\text{m}$ , constant length  $2\ \text{mm}$  and variable widths in the range  $10\text{--}50\ \mu\text{m}$ . The Hall probe was scanned above the sample at an estimated height of  $25 \pm 3\ \mu\text{m}$  (Hall probe active area size =  $4 \times 4\ \mu\text{m}^2$ , measurement step size along  $y$  is  $5\ \mu\text{m}$ ).

The 2D image and two one-dimensional (1D) profiles of the out-of-plane magnetic field component, measured by the SHPM are shown in Fig. 4. The profile in Fig. 4(a) corresponds to a scan made towards the center of the motif while the profile in Fig. 4(c) corresponds to a position close to the bottom edge of the motif. The 1D profiles show that the amplitude of the magnetic field produced at a given height above the sample decreases as the feature width decreases. Features as small as  $15\ \mu\text{m}$  are resolved at a scan height of  $25\ \mu\text{m}$ . The measured profiles have a vertical off-set, the magnitude of which is greater for the measurement made near the bottom edge of the motif.

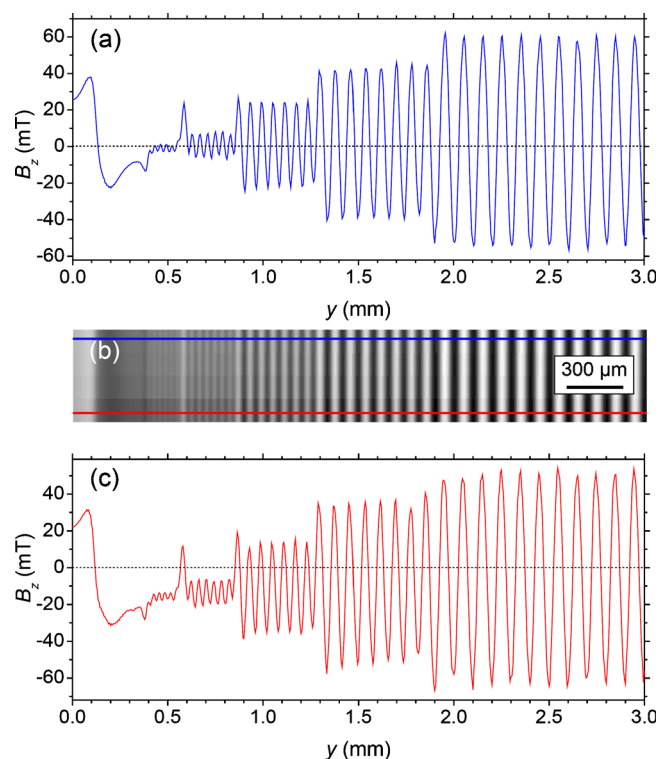


FIG. 4. (Color online) 2D image (b) and 1D profiles of the out-of-plane magnetic field component of topographically patterned  $38\ \mu\text{m}$  thick NdFeB film unidirectionally magnetized out-of-plane measured towards the center of the motif (a) and near the edge of the motif (c).

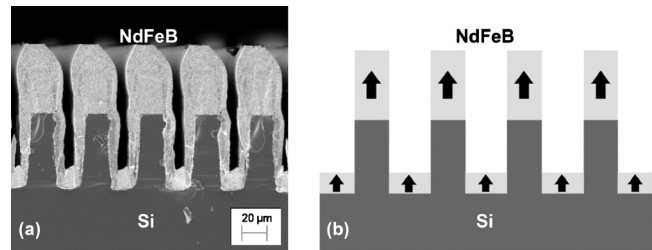


FIG. 5. (a) SEM image of the fractured cross-section of a  $38\ \mu\text{m}$  thick NdFeB film deposited on a Si wafer patterned by DRIE (the film section shown here has  $20\ \mu\text{m}$  wide features); (b) schematic representation of the structure assumed for analytical calculation of the stray field patterns produced by the topographically patterned film (note that the deposit on the sidewalls is neglected).

The  $B_z/B_r$  profile at a height of  $25\ \mu\text{m}$  above the center of such a topographically patterned film, where  $B_r$  is the remanent induction of the magnetic material, was calculated analytically. The geometry of the modeled structure was based on a scanning electron microscope (SEM) image of the film's cross section, shown in Fig. 5(a). Assuming a parallelepiped shape for the magnets and neglecting the deposit on the sidewalls of the trenches, calculations were made either considering or neglecting the magnetic material deposited at the bottom of the trenches [Fig. 5(b)]. Note that the thickness of the sidewall deposit is only about  $5\ \mu\text{m}$  and its overall volume content becomes less significant as the feature width increases. The calculated profiles in Fig. 6 reveal that the bottom magnets contribute only to a slight shift in the vertical off-set of the  $B_z/B_r$  profile but to no appreciable difference in the peak-to-peak induction. The overall shape of the calculated profiles is in very good agreement with the measured profile [Fig. 4(a)], thus validating the assumptions made in modeling the structures. Calculations (not shown here) demonstrate that the vertical off-set in the field values has two contributions: (i) the nonpatterned film sections in proximity to the patterned motif and (ii) the finite length of the motif's features. This explains why the vertical off-set is stronger in the profile measured at the edge of the motif than that measured towards the center of the motif.

The calculations and measurements show that both peak-to-peak magnetic field values,  $B_z^{\text{p-p}}$ , and the ratio  $B_z^{\text{p-p}}/B_r^{\text{p-p}}$  ( $50\ \mu\text{m}$ )/ $B_r^{\text{p-p}}$  normalized for features of different widths with respect to the widest  $50\ \mu\text{m}$  one vary with the distance

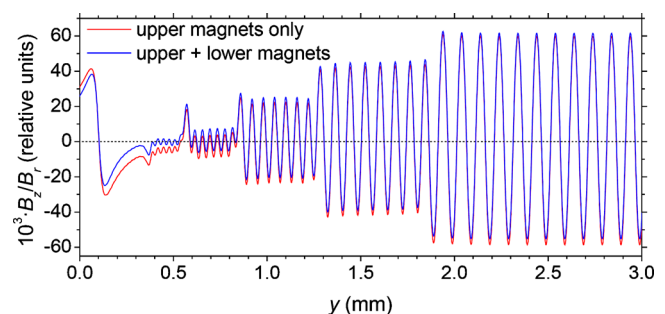


FIG. 6. (Color online) Calculated 1D profiles of the out-of-plane magnetic field component along the center of the motif, normalized to the value of remanent induction of the magnetic material, assuming a scan height of  $25\ \mu\text{m}$ .

TABLE I. Calculated and measured maximum, minimum, and peak-to-peak values of the  $z$ -component of the magnetic field above features of different widths; relative values normalized with respect to the 50  $\mu\text{m}$  wide feature are also given.

	Distance above feature ( $\mu\text{m}$ )	Feature width ( $\mu\text{m}$ )	$B_z^{\text{max}}$ (mT)	$B_z^{\text{min}}$ (mT)	$B_z^{\text{p-p}}$ (mT)	$B_z^{\text{p-p}}(50)/B_z^{\text{p-p}}$
Calculated	20	50	78	-82	160	1
		40	62	-62	124	1.3
		30	37	-39	76	2.1
	25	20	9	-16	25	6.4
		50	56	-60	116	1
		40	42	-43	85	1.4
		30	22	-23	45	2.6
	30	20	2	-9	11	10.6
		50	42	-45	87	1
		40	28.5	-30	58.5	1.5
		30	12	-14.4	26.4	3.3
		20	0	-6	6	14.5
Measured	25 (estimated)	50	61	-54	115	1
		40	43	-39	82	1.4
		30	23	-22	45	2.6
		20	7.4	-6.2	13.6	8.5

above the films (Table I). The best agreement between experiment and calculation is achieved for the calculation which assumes a probe to sample distance of 25  $\mu\text{m}$  (Table I). This is in excellent agreement with the estimated sample to probe distance (see above).

A comparison between the measured and calculated peak-to-peak magnetic induction at the determined scan height of 25  $\mu\text{m}$  reveals that the average value of the remanent magnetization is about 1 T. This value is less than the value of 1.4 T, estimated for continuous (nonpatterned) films.<sup>11</sup> This reduction in the average value of remanence is attributed to local modifications in the crystallographic texture developed in films deposited on patterned substrates. Accordingly, both SEM imaging of the grain structure and a comparison between in-plane and out-of-plane hysteresis loops measured with an extraction magnetometer on an ensemble of motifs confirmed that these topographically patterned films are less well textured than continuous ones.<sup>25</sup>

## B. Characterization of thermomagnetically patterned films

The 2D distribution of the vertical (out-of-plane) component of the magnetic field produced by the thermomagnetically patterned film, measured by SHPM (Hall probe active area size= $40 \times 40 \mu\text{m}^2$ , measurement step size is 5  $\mu\text{m}$ ) at a height of approximately  $30 \pm 3 \mu\text{m}$  above its surface is shown in Fig. 7(a). The chosen step size was determined by a compromise between the image resolution and the measurement time. Note that the spatial resolution of the measurement device is lower than the step size (5  $\mu\text{m}$ ), for it depends also on the probe-sample distance (30  $\mu\text{m}$ ) and the size of the probe's active area ( $40 \times 40 \mu\text{m}^2$ ). The field profile measured along the line indicated in this image is plotted in Fig. 7(b). The faint dark traces observed on the white stripes in the 2D image are due to unintentional inter-

ference effects occurring during thermo-magnetic patterning.<sup>17</sup> The nonmonotonic variation in the peak intensities of the field profile can also be attributed to these interference effects. 2D distributions and field profiles at 30  $\mu\text{m}$  from the film surface were calculated assuming that the sections of the hard magnetic film reversed during thermo-magnetic patterning are parallelepiped in shape [Fig. 7(c)] and have the same value of remanent magnetization as the nonreversed sections, i.e., 1.4 T.<sup>11</sup> In addition, the width of the transition zone between reversed and nonreversed sections was assumed to be zero. A 2D distribution calculated using the known physical parameters of the patterned film (number of stripes, stripe length, area of nonreversed film surrounding the stripes) is shown in Fig. 7(d) and field profiles for different assumed depths of reversal are shown in Fig. 7(e).

The increase in the peak-to-peak height toward the edges of the pattern in Fig. 7(e) is due to the finite number of stripes while both the finite length of the stripes and the finite size of the nonreversed film surrounding the stripes lead to a vertical off-set. The overall shape of the calculated profiles [Fig. 7(e)] is in good agreement with the measured profile [Fig. 7(b)]. From the comparison between the peak-to-peak field values of the experimental and calculated field profiles it is deduced that approximately  $1.3 \pm 0.2 \mu\text{m}$  of the film was reversed during thermomagnetic patterning. The 15% error in this evaluation is due to (i) the uncertainty in the estimate of the probe to sample distance and (ii) to the fact that the reversed volume was assumed to be a parallelepiped. This reversal depth agrees relatively well with the value of  $1.2 \pm 0.3 \mu\text{m}$ , estimated by comparing the average remanent magnetization of the as-irradiated film ( $M_r^i$ ) with the average remanent magnetization measured following saturation in a field of 8 T ( $M_r^s$ ), measured in a vibrating sample

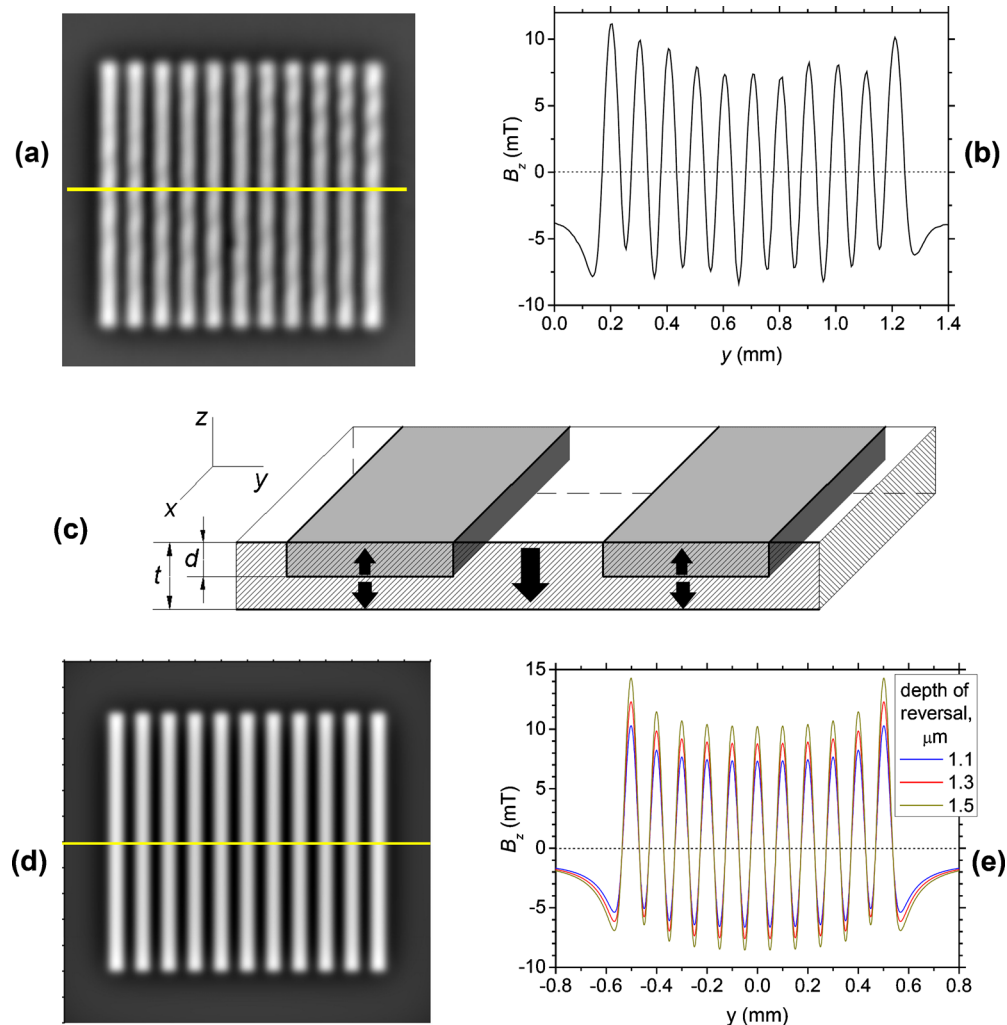


FIG. 7. (Color online) (a) SHPM image of the out of plane component of the magnetic field pattern measured at  $30 \mu\text{m}$  above the surface of a thermomagnetically patterned  $4 \mu\text{m}$  thick Nd-Fe-B film. (b) Field profile along the line indicated in (a). (c) Schematic representation of the structure assumed for analytical calculation of the stray field patterns produced by the thermo-magnetically patterned film. (d) Analytically simulated 2D image of the sample with the parameters as in (a). (e) 1D field profiles of (d) calculated for different assumed depths of magnetization reversal.

magnetometer.<sup>17</sup> Note that when the finite size of the Hall sensor active area is not taken into account, the reversal depth is estimated to be  $1.1 \pm 0.2 \mu\text{m}$ .<sup>17</sup>

### C. Derivation of the field and field gradients produced at different heights above the micropatterned hard magnetic films

The micromagnet arrays reported here are of particular interest for lab-on-chip applications, such as the trapping of biological species (liposomes, cells, bacteria, etc.) tagged with magnetic nanoparticles,<sup>32</sup> or the levitation/confinement of diamagnetic objects (cells, water droplets, etc.).<sup>33,34</sup> The strength of the field and the field gradient produced by a hard magnet varies strongly with distance from the magnet and it is important to quantify these parameters at the relevant length scales. The values of the  $z$ -component of the magnetic field, measured at one given sample-to-probe distance, have been used to derive the modulus of the magnetic field ( $B = |\mathbf{B}| \equiv \sqrt{B_x^2 + B_y^2 + B_z^2}$ ), and two components of its gradient:  $\partial B / \partial z$  and  $\partial B / \partial y$  at three different distances (0.1, 1, and  $10 \mu\text{m}$ ) above the micromagnet arrays (Fig. 8). These dis-

tances were chosen because the typical size of the magnetic nanoparticles used for tagging is in the range 10–100 nm, while that of bacteria and cells is of the order of  $1 \mu\text{m}$  and  $10 \mu\text{m}$ , respectively. The calculations were made above the central micromagnet, with the entire array being taken into consideration (in the case of the topographically patterned film, the calculation was made above the central  $50 \mu\text{m}$  wide micromagnet). In the calculations the same assumptions concerning the micromagnet geometry described in Secs. III A and III B were made.

The idealized straight-walled sharp-cornered geometry most probably leads to an overestimation of the values of field and field gradient, especially at the closest distance. Nevertheless the comparison of fields and field gradients at different heights above the structures may be considered to be instructive. In future work finite element analysis will be used to simulate structures that emulate the observed structure shape.

At the closest distance of  $0.1 \mu\text{m}$ , the values of the field modulus and field gradients are maximum for the thermomagnetically patterned film ( $B = 1.1 \text{ T}$ ;  $\partial B / \partial z = -4.1$

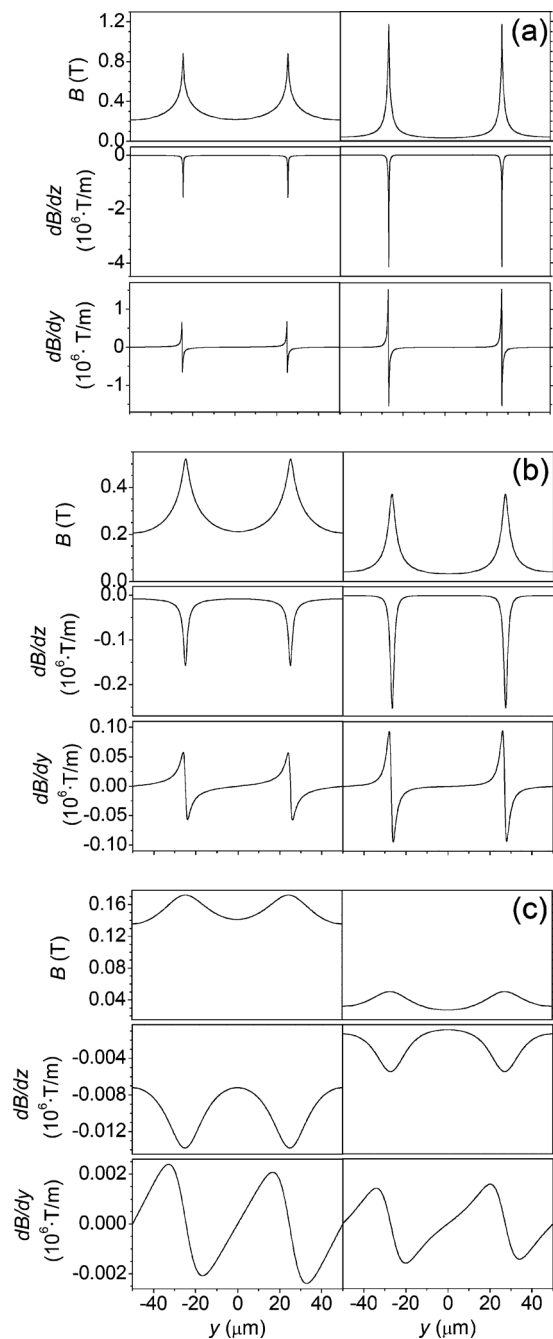


FIG. 8.  $B$ ,  $\partial B/\partial z$ , and  $\partial B/\partial y$  profiles calculated at distances  $z=0.1$ ,  $1$ , and  $10$   $\mu\text{m}$  [(a), (b), and (c), respectively] above the central micromagnet, with the entire array being taken into consideration; left hand column—topographically patterned film of thickness  $38$   $\mu\text{m}$  (above the central  $50$   $\mu\text{m}$  wide micromagnet), right hand column—thermomagnetically patterned film of effective thickness  $1.3$   $\mu\text{m}$ .

$\times 10^6$  T/m;  $\partial B/\partial y = \pm 1.5 \times 10^6$  T/m). For both structures significant fields and gradients are produced only at the edges of the micromagnets, because of the effect of nonuniform demagnetizing field distributions inherent in nonellipsoidal bodies.<sup>35</sup> At larger distances ( $1$   $\mu\text{m}$  and  $10$   $\mu\text{m}$ ), the value of the field modulus is greater for the topographically patterned film (maximum values:  $0.5$  T and  $0.016$  T, respectively). Only for the largest distance ( $10$   $\mu\text{m}$ ), the field gradients are maximum for the topographically patterned film ( $\partial B/\partial z = -0.014 \times 10^6$  T/m;  $\partial B/\partial y = \pm 0.002 \times 10^6$  T/m).

This disparity reflects (i) the difference in film thickness ( $38$   $\mu\text{m}$  and  $1.3$   $\mu\text{m}$  for the topographically and thermomagnetically patterned films, respectively), and (ii) the difference in their magnetic structure (the topographically patterned films are unidirectionally magnetized and physically separated by a gap, whereas thermomagnetically patterned micromagnets are oppositely magnetized and in direct contact, i.e., the structure is fully compact). The much greater thickness of the topographically patterned films only becomes important for the largest distance considered ( $10$   $\mu\text{m}$ ). In the case of trapping biological species tagged with magnetic nanoparticles, the thicker topographic films would act over a further distance, favoring the initial capture, while the bipolar thermomagnetically patterned magnets would better pin the trapped particles. Hybrid topographic-thermomagnetic structures could be used to optimize both the capture and trapping of magnetic nanoparticles.

#### IV. CONCLUSIONS

SHPM has been used for the quantitative measurement of the stray magnetic fields produced by micropatterned high performance hard magnetic films. Comparison of experimentally measured field patterns with calculated ones provides important information concerning the micromagnets' internal magnetic structure. In the case of topographically patterned films, estimation of the average value of remanent magnetization revealed that deposition onto patterned substrates influenced the crystallographic texture achieved. In the case of thermo-magnetically patterned films, the depth of magnetization reversal was estimated. SHPM is a direct, nondestructive method, with a good compromise between spatial resolution and measurement range, which is well suited for quality control of batch fabricated micromagnets and it can be used to optimize the design of microsystems incorporating such magnets. The patterned films characterized in this study generate fields with peak-to-peak  $z$ -component induction values in the range  $20$ – $120$  mT at heights of  $25$ – $30$   $\mu\text{m}$  above the micromagnet arrays. At these distances the field gradient values are of the order of  $10^3$  T/m increasing up to  $10^6$  T/m at the magnet surface. A comparison of the derived  $z$ -dependence of the field and field gradient profiles reveals the relative importance of the film thickness on one hand and the magnetic structure (noncompact unipolar structure versus fully-compact bipolar structure) on the other hand. The use of these micromagnet arrays for the trapping and confinement of magnetic micro-objects is now being studied for lab-on-chip applications.

#### ACKNOWLEDGMENTS

The authors gratefully acknowledge the RTRA Fondation Nanosciences for financial support of this work. One of the authors (R.G.) acknowledges support of the Federal Target Program "Scientific and Scientific-Pedagogical Personnel of Innovative Russia for the period 2009–2013." The DRIE was performed at the PTA/MINATEC.

<sup>1</sup>J. Y. Park and M. G. Allen, *J. Micromech. Microeng.* **8**, 307 (1998).

<sup>2</sup>T. S. Chin, *J. Magn. Magn. Mater.* **209**, 75 (2000).

<sup>3</sup>J. W. Judy, *Smart Mater. Struct.* **10**, 1115 (2001).

- <sup>4</sup>O. Cugat, J. Delamare, and G. Reyne, *IEEE Trans. Magn.* **39**, 3607 (2003).
- <sup>5</sup>D. P. Arnold, *IEEE Trans. Magn.* **43**, 3940 (2007).
- <sup>6</sup>K. W. Oh and C. H. Ahn, *Comprehensive Microsystems* (Elsevier, New York, 2008), Vol. 2, p. 39.
- <sup>7</sup>R. P. Allen, S. D. Dahlgren, H. W. Arrowsmith, and J. P. Heinrich, AFML Technical Report No. AFML-TR-74-87, 1974.
- <sup>8</sup>F. J. Cadieu, *J. Vac. Sci. Technol. A* **6**, 1668 (1988).
- <sup>9</sup>F. J. Cadieu, in *Physics of Thin Films*, edited by M. Francombe and J. Vossen (Academic, New York, 1992), Vol. 16.
- <sup>10</sup>B. A. Kapitanov, N. V. Kornilov, Y. L. Linetsky, and V. Y. Tsvetkov, *J. Magn. Magn. Mater.* **127**, 289 (1993).
- <sup>11</sup>N. M. Dempsey, A. Walther, F. May, D. Givord, K. Khlopkov, and O. Gutfleisch, *Appl. Phys. Lett.* **90**, 092509 (2007).
- <sup>12</sup>A. Walther, K. Khlopkov, O. Gutfleisch, D. Givord, and N. M. Dempsey, *J. Magn. Magn. Mater.* **316**, 174 (2007).
- <sup>13</sup>H. Lemke, T. Lang, T. Giiddhenrich, and C. Heiden, *J. Magn. Magn. Mater.* **148**, 426 (1995).
- <sup>14</sup>T. Budde and H. H. Gatzel, *J. Appl. Phys.* **99**, 08N304 (2006).
- <sup>15</sup>J. Zhang, Y. K. Takahashi, R. Gopalan, and K. Hono, *J. Magn. Magn. Mater.* **310**, 1 (2007).
- <sup>16</sup>A. Walther, C. Marcoux, B. Desloges, R. Grechishkin, D. Givord, and N. M. Dempsey, *J. Magn. Magn. Mater.* **321**, 590 (2009).
- <sup>17</sup>F. Dumas-Bouchiat, L. F. Zanini, M. Kustov, N. M. Dempsey, R. Grechishkin, K. Hasselbach, J. C. Orlianges, C. Champeaux, A. Catherinot, and D. Givord, *Appl. Phys. Lett.* **96**, 102511 (2010).
- <sup>18</sup>R. M. Grechishkin, S. Chigirinsky, M. Gusev, O. Cugat, and N. M. Dempsey, in *Magnetic Nanostructures in Modern Technology*, edited by B. Azzerboni, G. Asti, L. Pareti, and M. Ghidini (Springer/Kluwer Academic, Dordrecht, 2007), pp. 195–224.
- <sup>19</sup>A. M. Chang, H. D. Hallen, L. Harriott, H. F. Hess, H. L. Kao, J. Kwo, R. E. Miller, R. Wolfe, J. van der Ziel, and T. Y. Chang, *Appl. Phys. Lett.* **61**, 1974 (1992).
- <sup>20</sup>A. Oral, S. J. Bending, and M. Henini, *Appl. Phys. Lett.* **69**, 1324 (1996).
- <sup>21</sup>R. B. Dinner, M. R. Beasley, and K. A. Moler, *Rev. Sci. Instrum.* **76**, 103702 (2005).
- <sup>22</sup>O. Kazakova, J. Gallop, G. Perkins, and L. Cohen, *Appl. Phys. Lett.* **90**, 162502 (2007).
- <sup>23</sup>S. Schnittger, S. Dreyer, Ch. Jooss, S. Sievers, and U. Siegner, *Appl. Phys. Lett.* **90**, 042506 (2007).
- <sup>24</sup>S. Chigirinsky, M. Kustov, N. Dempsey, C. Ndao, and R. Grechishkin, *Rev. Adv. Mater. Sci.* **20**, 85 (2009).
- <sup>25</sup>D. O'Brien *et al.* (unpublished).
- <sup>26</sup>A. Pross, A. I. Crisan, S. J. Bending, V. Mosser, and M. Konczykowski, *J. Appl. Phys.* **97**, 096105 (2005).
- <sup>27</sup>The quantum well Hall sensors (QWHSs) based on AlGaAs/InGaAs/GaAs heterostructures were provided by V. Mosser of Itron SAS, France.
- <sup>28</sup>K. Hasselbach, C. Ladam, V. O. Dolocan, D. Hykel, T. Crozes, K. Schuster, and D. Mailly, *J. Phys. Conf. Ser.* **97**, 012330 (2008).
- <sup>29</sup>E. M. Purcell, *Electricity and Magnetism*, Berkeley Physics Course Vol. II (McGraw-Hill, New York, 1986).
- <sup>30</sup>R. M. Grechishkin, L. E. Afanasieva, Y. G. Pastushenkov, and N. N. Maksimov, *Meas. Sci. Technol.* **5**, 853 (1994).
- <sup>31</sup>N. Takahashi, K. Akiyama, H. Kato, and K. Kishi, *COMPEL: The International Journal of Computation and Mathematics in Electrical and Electronic Engineering* **27**, 144 (2008).
- <sup>32</sup>M. A. M. Gijs, *Microfluidic Technologies for Miniaturized Analysis Systems* (Springer, USA, 2007), pp. 241–274.
- <sup>33</sup>I. F. Lyuksyutov, D. G. Naugle, and K. D. D. Rathnayaka, *Appl. Phys. Lett.* **85**, 1817 (2004).
- <sup>34</sup>M. Frénéa-Robin, H. Chetouani, N. Haddour, H. Rostaing, J. Laforêt, and G. Reyne, 30th IEEE EMBS Annual International Conference, Vancouver, BC, Canada, 20–25 August 2008 (IEEE, New York, 2008), pp. 3360–3363.
- <sup>35</sup>R. I. Joseph and E. Schlomann, *J. Appl. Phys.* **36**, 1579 (1965).